Multilayer stacking ferroelectricity in two-dimensional materials with Bravais lattice symmetry: Theory and applications

Jiaqi Xin [1,2] Yaguang Guo [1,2,*] and Qian Wang [3]

[1] *Department of Physics, School of Physical Science and Engineering, Beijing Jiaotong University, Beijing 100044, China*

[2] *Beijing Key Laboratory of Novel Materials Genetic Engineering and Application for Rail Transit, Beijing Jiaotong University, Beijing 100044, China*

[3] *School of Materials Science and Engineering, Peking University, Beijing 100871, China*

(Received 27 November 2025; revised 25 January 2026; accepted 10 February 2026; published 25 February 2026)

The sliding of van der Waals (vdW) bilayers can induce electric polarization in certain nonpolar two-dimensional (2D) materials. However, this mechanism does not apply to 2D materials with Bravais lattice symmetry (e.g., graphene), where the atomic structure and lattice symmetry have the same point group, preserving inversion symmetry across all stacking configurations. To overcome this limitation, multilayered vdW structures can be exploited for their diverse structural symmetries. In this work, we present a general theory for multilayer stacking ferroelectricity (MSF), which systematically analyzes whether and how different types of polarization can emerge in vdW multilayers composed of 2D materials with Bravais lattice symmetry. This theory clarifies the symmetry evolution during stacking and unifies previous work on sliding ferroelectrics, including tetralayer graphene. Guided by the MSF theory, we design a ferroelectric trilayer C_3N that exhibits multidirectional in-plane polarization, inducing a strong bulk photovoltaic effect (BPVE) coupled with the ferroelectric order, which is absent in both monolayer and bilayer. These findings highlight the importance of the MSF theory in the design of 2D ferroelectrics for ferroelectric photovoltaic applications.

DOI: 10.1103/9tt5-qm26

I. INTRODUCTION

The emergence of ferroelectricity in materials is fundamentally driven by symmetry breaking in their crystal structures. This symmetry requirement severely limits the number of 2D ferroelectric materials that have been experimentally confirmed, with only a few examples reported to date, including $CuInP_2S_6$ [1,2], α-In_2Se_3 [3–5], $MoTe_2$ [6], bismuth [7], etc. In 2017, Li *et al.* proposed that, for most 2D nonpolar materials, symmetry can be effectively reduced at the interface in their van der Waals (vdW) stacked bilayers, hence enabling the emergence of electric polarization, which can be switched by interlayer sliding [8]. Since then, sliding ferroelectricity has been experimentally observed in several vdW stacked bilayers, such as h-BN [9–11] and transition metal dichalcogenides (TMDs) [12–21], showing great potential for applications in high-speed nonvolatile memory [22], ferroelectric photovoltaics [23–26], and so on.

However, such a mechanism is not applicable to all 2D materials. A notable example is graphene, whose bilayer is nonferroelectric upon any stacking configuration [27,28]. This can be understood from the recently proposed theory for bilayer stacking ferroelectricity (BSF) [29,30], which states that for a stacked bilayer with unchanged unit cell size, the interlayer rotation must correspond to one of the elements of the monolayer lattice's symmetry group. In graphene, both its hexagonal lattice and the honeycomb atomic structure possess the D_{6h} point group (PG) symmetry, implying that no rotational operation can change the relative orientation between the two graphene layers. As a result, when two graphene sheets are stacked with aligned orientation, no matter how they are translated with each other, the bilayer remains centrosymmetric, and hence is nonpolar. As we know, there are five 2D Bravais lattices [31]: primitive oblique (oP-C_{2h}), primitive rectangular (rP-D_{2h}), centered rectangular (rC-D_{2h}), primitive square (sP-D_{4h}), and primitive hexagonal (hP-D_{6h}). The abbreviations for these five categories and their corresponding PG are given in parentheses. Similar to graphene, for any 2D material whose atomic structure shares the same symmetry as its Bravais lattice, electric polarization will be suppressed in all its bilayer configurations due to the conserved inversion symmetry.

To address this issue, one possible approach is to explore electric polarization in multilayer vdW stacks. As the number of layers increases, the variety of possible stacking configurations also grows, leading to greater diversity in structural symmetry. For example, although the AB-stacked graphene bilayer is centrosymmetric, the inversion symmetry can be readily removed in the ABA-stacked graphene trilayer, which therefore exhibits a strong second harmonic generation (SHG) response [28]. Furthermore, in ABAC- and ABCB-stacked graphene tetralayers, the across-layer structural asymmetry leads to nonequivalent charge distributions along the out-of-plane direction, consequently giving rise to opposite polar states that can be electrically switched via sliding [27]. These studies suggest that the number of layers serves as a valuable degree of freedom for manipulating crystal symmetry and

*Contact author: ygguo@bjtu.edu.cn

electric polarization in 2D systems. Although graphene multilayers have been extensively studied [27,28,32–34], many other 2D materials with Bravais lattice symmetry remain unexplored, raising several questions that need to be solved. (1) For a given monolayer, whether polarization can be induced via multilayer stacking? If so, (2) what is the minimum number of layers required to induce polarization? (3) What types of polarization can emerge? (4) What stacking operators are necessary to achieve a particular polar state? To answer these questions, a general theory that governs the emergence of ferroelectricity in vdW multilayers is urgently needed.

In this work, we address these fundamental questions by developing a theoretical framework for multilayer stacking ferroelectricity (MSF). Using group theory analysis, we derive a general rule for the evolution of structural symmetry in vdW multilayers. This rule can be used to identify the possible polar states in multilayers stacked from monolayers with Bravais lattice symmetry. We validate the proposed MSF theory by revisiting the previous findings in multilayer graphene. We further design a ferroelectric trilayer based on monolayer C_3N, which exhibits multidirectional polar states. Interestingly, we find a strong bulk photovoltaic effect (BPVE) in such a ferroelectric trilayer, where the shift current can couple with the ferroelectric order, holding the potential for switchable photoelectric device applications.

II. COMPUTATIONAL DETAILS

First-principles calculations are performed using the Vienna *ab initio* simulation package [35] with the projector augmented wave approach [36]. The exchange-correlation potential is treated with the Perdew-Burke-Ernzerhof functional [37] within the generalized gradient approximation. A plane-wave energy cutoff of 500 eV and a Monkhorst-Pack $\boldsymbol{k}$-point grid [38] with spacing of $2\pi \times 0.01$ Å^{-1} are adopted. The C_3N configurations are fully relaxed until forces are less than 0.01 eV Å^{-1} and energy changes are less than 1×10^{-4} eV. The Berry phase method [39] is used to calculate electric polarization, while the sliding energy barriers are calculated by using the climbing image nudged elastic band method [40]. The vdW interactions are considered by using the DFT-D3 method. The shift current responses are obtained using Wannier interpolation [41], based on maximally localized Wannier functions constructed via WANNIER90 [42] with a $71\times71\times1$ $\boldsymbol{k}$-point sampling (see Sec. IV of the Supplemental Material [43] for detailed Wannierization parameters and $\boldsymbol{k}$-mesh convergence test).

III. RESULTS AND DISCUSSION

A. Symmetry evolution in multilayer stacking

According to Neumann's principle, the polarization of a 2D system remains invariant under the action of its PG symmetry operators [44]. Therefore, once the PG of the multilayer structure is determined, the allowed polar states can be subsequently identified by all constrains collected from the PG elements. This needs us to understand the symmetry evolution when constructing a N-layer system (denoted as M_N) from the corresponding monolayer. In the following, we use G_N to represent the layer group (LG) of a N-layer structure with $\hat{R}_N$ as the element in G_N, i.e., $G_N = \{\hat{R}_N\}$. Note that $\hat{R}_N = \{R_N|\tau_N\}$ is composed of a rotational part R_N and an in-plane translational part τ_N [45].

We begin with the trilayer (M_3). It is known that applying any symmetry operator $\hat{R}_3$ in G_3 on the M_3 structure would keep itself unchanged [see Fig. 1(a)], which means that the middle layer S would also stay the same under the action of these symmetry operators. Thus G_3 must be a subgroup of the LG for the monolayer (i.e., G_1). In other words, when a monolayer is stacked into a trilayer, it is only accompanied by the breaking of the original symmetries without any new symmetry introduced. Similarly, for a stacked tetralayer (M_4), any symmetry operator $\hat{R}_4$ in G_4 preserves the M_4 structure [see Fig. 1(b)], hence the internal bilayer ($B = S + S'$) also remains unchanged under the action of these operators, indicating that G_4 is a subgroup of the LG for the bilayer (i.e., G_2). Inspired by these two cases, one can construct a M_N structure by adding two new layers (S_1 and S_2) at the top and bottom of M_{N-2} [see Fig. 1(c)]. Any symmetry operator in G_N can keep the configuration of M_{N-2} unchanged, therefore G_N must belong to G_{N-2}, i.e., $G_N \subseteq G_{N-2}$. Note that this recursive symmetry relationship between M_{N-2} and M_N is applicable to all 2D materials, regardless of whether they possess the Bravais lattice symmetry.

Based on the above discussion, the key question becomes how S_1 and S_2 affect the symmetry evolution from G_{N-2} to G_N. For bilayer stacking, it has only one interface, whose configuration can be described by a stacking operator $\hat{\tau}_z\hat{O}$ between two layers. Here, $\hat{\tau}_z = \{E|\tau_z\}$ is an out-of-plane translation that does not affect the bilayer symmetry, and $\hat{O} = \{O|\tau_O\}$ is a transformation operator comprising a rotational part O and an in-plane translational part τ_O. Thus the bilayer symmetry is solely determined by the action of O and τ_O on monolayer symmetry [29,30]. However, constructing M_N from M_{N-2} involves two interfaces, which requires two stacking operators $\hat{\tau}_{z1}\hat{O}_1$ and $\hat{\tau}_{z2}\hat{O}_2$ with six variables O_1, O_2, τ_{O1}, τ_{O2}, τ_{z1} and τ_{z2} for description [see Fig. 1(c)]. If we consider all these variables simultaneously, the number of possible combinations becomes infinite, making it difficult to develop a concise and physically intuitive theoretical framework. To address this challenge, in our theory, we set that all the adjacent two layers in M_N are stacked with an energetically favorable interfacial configuration. This setting means that the interfaces in M_N are all equivalent, and ensures that (1) the constructed M_N is more likely to be energetically stable, benefiting experimental feasibility; (2) the rotational operation is same for all interfaces, i.e., $O_1 = O_2$; (3) the values of τ_{z1} and τ_{z2} are identical, so that the interlayer distances do not affect G_N; (4) the possible values of τ_{O1} and τ_{O2} are constrained (see details in Sec. I of the Supplemental Material [43]). This setting is reasonable from the physical point of view. Since the 2D materials with Bravais lattice symmetry are nonpolar and lack intrinsic dipole moments, the electrostatic interaction between stacked layers is expected to be weak. For example, graphene prefers the so-called AB or BA stacking, and its tetralayer has four possible stable configurations including ABAB, ABAC, ABCA, and ABCB, where all adjacent layers adopt AB or BA stacking with in-plane translation restricted to (1/3, 2/3) or (2/3, 1/3) [27]. This setting is further supported by DFT calculations reported

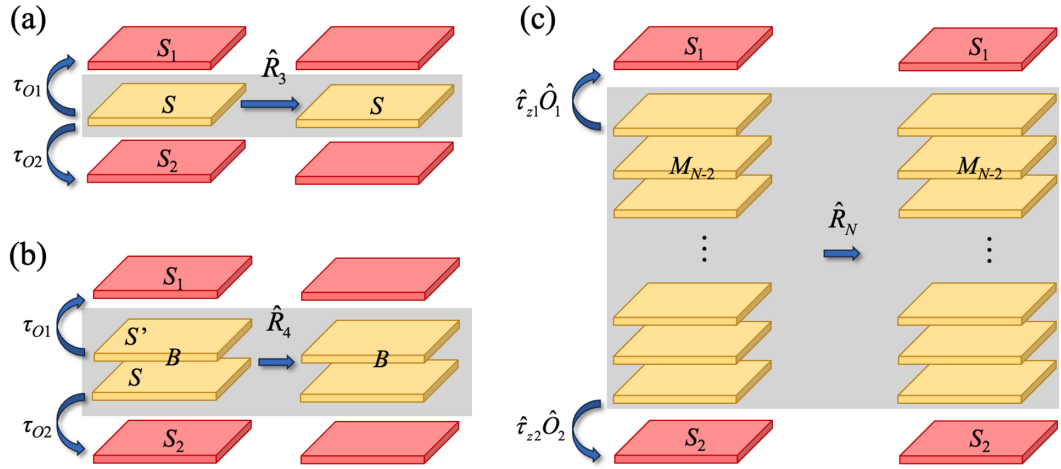

FIG. 1. (a) Effect of $\hat{R}_3$ acting on M_3 shows that $G_3 \subseteq G_S$. (b) Effect of $\hat{R}_4$ acting on M_4 shows that $G_4 \subseteq G_B$. (c) M_N can be viewed as the result of adding S_1 and S_2 to the top and bottom of M_{N-2}, therefore we obtain $G_N \subseteq G_{N-2}$.

in subsequent studies of the multilayer C_3N system (see Fig. S10 [43]). Note that when this framework is applied to more strongly coupled systems with significant electrostatic interactions, it is suggested to examine the relative stability of different stacking configurations using DFT calculations. Within this setting, the number of variables can be reduced and the originally combined variables can be separated. Moreover, for 2D materials with Bravais lattice symmetry, the rotation between two stacked adjacent layers is the identity operator, i.e., $O_1 = O_2 = E$, thus it only needs to consider the influence of in-plane translation τ_{O1} and τ_{O2} on the symmetry evolution from G_{N-2} to G_N.

We first investigate the case of trilayer ($M_3 = S_1 + S + S_2$). Here, τ_{O1} and τ_{O2} represent the in-plane translations from S to S_1 and S_2, respectively [see Fig. 1(a)], satisfying $S_i = \hat{\tau}_{zi}\hat{O}_i S = S + \tau_{Oi} + \tau_{zi} (i \in \{1, 2\})$. Note that symmetry operators in 2D systems can be classified into two types based on whether they invert the z-coordinates of atoms, distinguished by superscripts "+" and "–" [29,30]. According to this classification, for a symmetry operator $\hat{R}_3 = \{R_3|\tau_3\} \in G_3$, $\hat{R}_3^-$ exchanges the positions of S_1 and S_2 and leaves S unchanged, whereas $\hat{R}_3^+$ preserves the stacking order for all three layers. Here, $\hat{R}_3^\pm$ must satisfy the following equation:

$$\begin{pmatrix} R_{11} & R_{12} & 0 \\ R_{21} & R_{22} & 0 \\ 0 & 0 & R_{33} \end{pmatrix} \begin{pmatrix} \tau_{Oix} \\ \tau_{Oiy} \\ 0 \end{pmatrix} = \begin{pmatrix} \tau_{Ojx} + n_1 \\ \tau_{Ojy} + n_2 \\ 0 \end{pmatrix},$$

$$\begin{cases} i = j = 1, 2, & \text{when } R_{33} = 1 \\ i \neq j \in \{1, 2\}, & \text{when } R_{33} = -1 \end{cases}, \quad (1)$$

The detailed derivation is provided in Sec. II of Ref. [43]. Equation (1) takes the form of a linear system, where the 3×3 matrix represents R_3, with $R_{33} = 1$ (–1) corresponding to R_3^+ (R_3^-), respectively. The in-plane translation operators τ_{O1} and τ_{O2} are expressed as 3×1 vectors. For example, $\tau_{O1} = (1/3, 2/3, 0)^T$ indicates that S_1 is translated relative to S by (1/3, 2/3) of the lattice vectors. n_1 and n_2 are integers or half-integers that enforce translational invariance within the 2D periodic plane. Equation (1) can serve as a discriminant, i.e., once τ_{O1} and τ_{O2} are determined, the symmetry operators $\hat{R}_1$ in G_1 that satisfy Eq. (1) can be preserved when forming the LG of M_3 (i.e., G_3), while the others are annihilated during the stacking process. The derivation for tetralayer ($M_4 = S_1 + S + S' + S_2$) is also provided in Sec. II of Ref. [43], where τ_{O1} and τ_{O2} represent the in-plane translation from S' to S_1, and that from S to S_2, respectively [see Fig. 1(b)]. We find that Eq. (1) also serves as the discriminant for examining whether symmetry operators are preserved when constructing M_4 from a bilayer (see Sec. II of Ref. [43]). Since the symmetry of a bilayer can be directly obtained from the BSF theory [29,30], one can determine which elements are retained in M_4 by traversing all the elements in G_2. Based on the above discussion, the analysis of M_3 and M_4 can be directly extended to odd-layer (M_{odd}) and even-layer (M_{even}) stackings, following the sequences $S \to M_3 \to M_5 \to \cdots \to M_{\text{odd}}$ and $B \to M_4 \to M_6 \to \cdots \to M_{\text{even}}$, respectively.

B. Stacking-induced polar states

Next, we apply the theoretical framework established above, i.e., Eq. (1), to all 2D materials with Bravais lattice symmetry. All possible stacking-induced polarization behaviors are detailed in Sec. III of Ref. [43]. In Table I, we summarize the stacking-induced polar state combinations. The first column of Table I lists the possible combinations of the four polar states including out-of-plane polarization (OP), in-plane polarization (IP), combined polarization (CP) with both OP and IP components, and no polarization (NP) that may emerge in multilayer stackings, along with the corresponding conditions provided in each row. For example, the first row labeled "OP+NP" indicates that a stacked multilayer composed of 2D materials belonging to rC-D_{2h}, sP-D_{4h}, or hP-D_{6h} can exhibit both OP and NP when layer number $N \geqslant 4$, where the OP and NP states can be switched via interlayer sliding. In contrast, such a polar state combination cannot be realized at any layer number for oP-C_{2h} or rP-D_{2h}, as denoted by the "×." Other cases labeled by "IP+NP," "CP+NP," and "IP+CP+NP" are presented in a similar manner. One can see that some combinations such as "OP+IP+NP," "OP+CP+NP," or "OP+IP+CP+NP" do not appear, indicating that OP does not coexist with either IP or CP. This is because all configurations exhibiting "OP+NP"

TABLE I. Stacking-induced polar state combinations for five types of 2D materials with Bravais lattice symmetry. The numbers and the labels "even" or "odd" indicate the conditions on the layer number N under which the corresponding polar states emerge, while "×" denotes the absence of such states. G (0, 0), A (1/2, 0), B (0, 1/2), and C (1/2, 1/2) are translation points within the unit cell.

Polar state combinations	Conditions on	2D materials with Bravais lattice symmetry				
		oP-C_{2h}	rP-D_{2h}	rC-D_{2h}	sP-D_{4h}	hP-D_{6h}
OP+NP	layer number N	×	×	$\geqslant$4	$\geqslant$4	$\geqslant$4
IP+NP		=3	=3	=3	=3	=3
CP+NP		$\geqslant$4, even	$\geqslant$4, even	$\geqslant$4, even	$\geqslant$4, even	$\geqslant$4, even
IP+CP+NP		$\geqslant$5, odd	$\geqslant$5, odd	$\geqslant$5, odd	$\geqslant$3, odd	$\geqslant$3, odd
NP	τ_{O1} and τ_{O2}	G, A, B, C	G, A, B, C	$G(C), A(B)$	G, C	G

preserve the out-of-plane rotational axes, which inhibit the emergence of IP. The last row labeled "NP" corresponds to cases where electric polarization cannot be induced. When both τ_{O1} and τ_{O2} are located at one of the in-plane translational points G (0, 0), A (1/2, 0), B (0, 1/2), or C (1/2, 1/2), all resulting stackings preserve the monolayer PG, thereby remaining centrosymmetric and nonpolar. A notable example is monolayer black phosphorus (BP), which belongs to rP-D_{2h}. For its ground-state stackings, adjacent layers are shifted by an in-plane translation of (0, 1/2) [46]. As a result, all BP multilayer stackings, including ABA-stacked trilayer and ABAB-stacked tetralayer, retain the D_{2h} symmetry and do not exhibit spontaneous electric polarization.

In addition to the information summarized in Table I, two key findings are noteworthy. First, with the exception of the cases listed in the last row, inversion symmetry in 2D materials with Bravais lattice symmetry can always be broken through vdW stacking when $N \geqslant 3$. This finding establishes a direct relationship between stacking engineering and inversion-symmetry breaking, thereby offering theoretical guidance for the design of non-centro-symmetric systems and providing insights into experimental observations, e.g., SHG in ABA-stacked graphene trilayer [28]. Second, since stacking can only reduce the number of symmetry operators, the symmetry evolution in multilayer stackings would converge when $N \geqslant 4$ for M_{even} and $N \geqslant 5$ for M_{odd} (see Figs. S2–S6 of Ref. [43]). Beyond these thresholds, all possible PGs and polar states remain invariant when N further increases. This convergence delineates a symmetry scope for multilayer stacking, which can be characterized through few-layer structures, and serves as a foundation for systematic investigations of symmetry-governed physical properties and practical applications.

C. MSF in graphene and C_3N

We now apply the MSF theory to explain the symmetry evolution of stacked graphene multilayers, thereby validating our theoretical framework. Monolayer graphene belongs to hP-D_{6h}. For its energy-favorable AB- or BA-stacking, the two adjacent layers are shifted by an in-plane translation of (1/3, 2/3) or (2/3, 1/3). The detailed evolution of PGs is illustrated as type 2 in Fig. S6 of Ref. [43]. When constructing vdW multilayers, there are two possible combinations for τ_{O1} and τ_{O2}: (1) $\tau_{O1} = \tau_{O2} =$ (1/3, 2/3) or (2/3, 1/3), which preserves symmetry operators in D_{3h} while annihilating the rest of D_{6h}; (2) $\tau_{O1} =$(1/3, 2/3) and $\tau_{O2} =$ (2/3, 1/3) (or vice versa), which preserves symmetry operators in D_{3d} while annihilating the rest of D_{6h}.

Based on this, two distinct stacking configurations arise from monolayer to trilayer: ABC stacking (D_{3d}) for $\tau_{O1} \neq \tau_{O2}$, and ABA stacking (D_{3h}) for $\tau_{O1} = \tau_{O2}$. ABC stacking is centrosymmetric and nonpolar, as the inversion symmetry is preserved in D_{3d}. In contrast, ABA stacking lacks inversion symmetry, enabling the strong SHG response observed experimentally [28]. However, due to the coexistence of the out-of-plane three-fold rotational axis and in-plane mirror in D_{3h}, ABA stacking remains nonpolar. Therefore more graphene layer is needed to further remove those symmetries to induce electric polarization. Now consider tetralayer graphene. Bilayer graphene belongs to the D_{3d} PG [29]. From bilayer to tetralayer, when $\tau_{O1} \neq \tau_{O2}$, the resulting configurations (ABAB and ABCA) preserve the D_{3d} symmetry exhibiting NP. In contrast, when $\tau_{O1} = \tau_{O2}$, the PG of the resulting configurations (ABAC and ABCB) reduces to the intersection of D_{3h} and D_{3d}, namely C_{3v}. In this case, all R^- symmetry operators, including inversion, are broken, which is structurally manifested as across-layer asymmetry: ABAC stacking corresponds to AA stacking for the first through third layer and AB stacking for the second through fourth layer, while it is reversed in ABCB stacking [27]. Such out-of-plane asymmetry enables the emergence of OP along the three-fold rotational axis in C_{3v}. Overall, tetralayer graphene can exhibit the "OP+NP" polar state combination, as shown in Table I. Based on the same analysis, OP can also be induced from M_3 to M_5. Notably, all symmetry operators in C_{3v} are preserved regardless of whether τ_{O1} equals to τ_{O2}, making C_{3v} the minimal PG for multilayer graphene. Consequently, the symmetry evolution in multilayer graphene is ultimately confined to the framework $\{D_{3d}$ and $C_{3v}\}$ when $N \geqslant 4$ for M_{even}, and $\{D_{3d}, D_{3h}, C_{3v}\}$ when $N \geqslant 5$ for M_{odd}. These results are consistent with early studies [32–34], hence validating the reliability of the MSF theory.

As shown in Table I, in addition to OP, 2D materials belonging to hP-D_{6h} can also exhibit IP when stacked into a trilayer. According to our theory, this requires that the energy-favorable in-plane translation between adjacent layers deviates from (1/3, 2/3) and (2/3, 1/3) (see Fig. S6 of Ref. [43]). We now study the polar states in a C_3N trilayer. Monolayer C_3N can be regarded as graphene uniformly doped with nitrogen atoms, hence belonging to hP-D_{6h} as well [47–50]. Previous experiment revealed that the

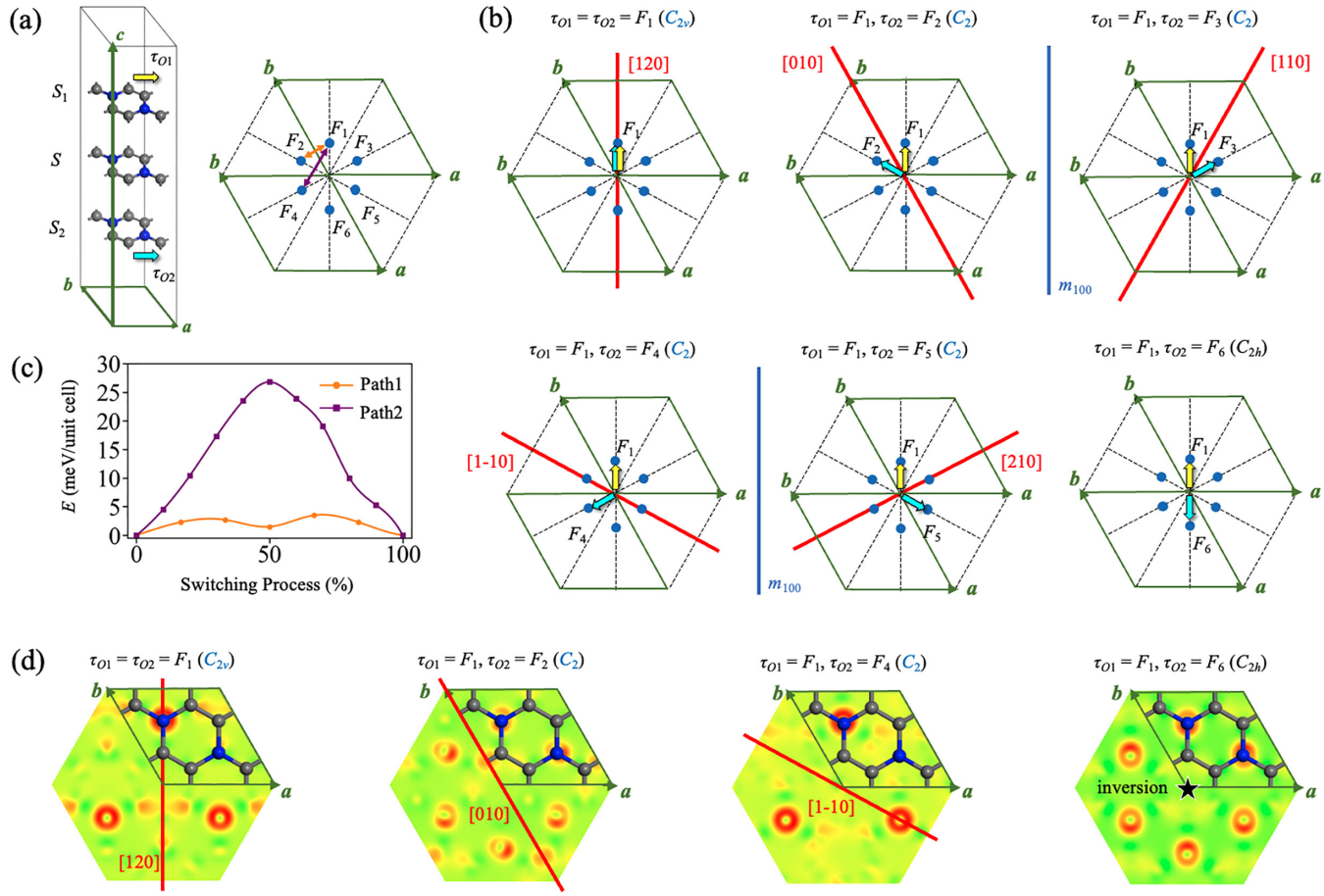

FIG. 2. (a) Schematic illustration of trilayer C_3N and the six equivalent translation points. (b) Six distinct configurations trilayer C_3N. Red lines represent the twofold rotational axes. Yellow and cyan arrows indicate τ_{O1} and τ_{O2}, respectively. (c) Energy variation of trilayer C_3N along two representative sliding pathways, path1 (orange) and path2 (purple), corresponding to sliding the bottom layer S_2 from F_1 to F_2, and from F_1 to F_4, respectively. (d) Charge density difference ($\Delta\rho$) on the slice corresponding to the middle layer S for trilayer C_3N in $\tau_{O2} = F_1$, F_2, F_4, and F_6 configurations. Red and green regions represent electron accumulation and depletion, respectively. The red lines indicate the orientations of the twofold rotation axes, and the black pentagram marks the inversion center.

interlayer translation for bilayer C_3N is (1/6, 1/3) [51], which corresponds to type 4 in Fig. S6 [43]. Therefore trilayer C_3N with such a stacking order can exhibit IP. According to Table S5 in Ref. [43], there are six degenerate translation points at the stacked C_3N interface: F_1 (1/6, 1/3), F_2 (–1/6, 1/6), F_3 (1/3, 1/6), F_4 (–1/3, –1/6), F_5 (1/6, –1/6), and F_6 (–1/6, –1/3), as shown in Fig. 2(a). By fixing $\tau_{O1} = F_1$ and varying τ_{O2} from F_1 to F_6, six distinct trilayer C_3N configurations can be constructed [Fig. 2(b)]: $\tau_{O2} = F_1$ corresponds to the one with C_{2v} symmetry exhibiting IP along [120] direction; $\tau_{O2} = F_2$, F_3, F_4, and F_5 correspond to those with C_2 symmetry exhibiting IP along [010], [110], [1–10], and [210] directions, respectively; $\tau_{O2} = F_6$ yields the C_{2h} symmetry and a nonpolar structure with an inversion center at the origin of the unit cell. The dynamical and thermal stability of the constructed C_3N trilayers is confirmed by phonon spectrum calculations and *ab initio* molecular dynamics simulations (see Figs. S11 and S12 in Sec. IV of Ref. [43]). The calculated polarization strengths are 27.10 pC/m for $\tau_{O2} = F_1$, 26.75 pC/m for $\tau_{O2} = F_2$ (F_3), and 27.07 pC/m for $\tau_{O2} = F_4$ (F_5), respectively, which are much larger than the OP strength in multilayer graphene [27]. Such an enhancement is closely correlated with enhanced charge transfer at the interface of trilayer C_3N (see Fig. S13 in Sec. IV of Ref. [43]). It can be seen that these polarizations have comparable magnitude of strength, but point in different directions, showing the multidirectional nature of ferroelectricity in trilayer C_3N. Switching among these polar states can be achieved by keeping the top (S_1) and middle (S) layers fixed, while sliding the bottom layer (S_2). Figure 2(c) shows the energy variation along two representative transition paths: the nearest-neighbor path1 ($F_1 \leftrightarrow F_2$) and the next-nearest-neighbor path2 ($F_1 \leftrightarrow F_4$), indicated by the orange and purple arrows in Fig. 2(a), respectively. Path1 is energetically favorable, with a transition barrier below 4 meV per unit cell. This value is comparable to that of tetralayer graphene (∼5 meV/unit cell) [27] and bilayer h-BN (8.8 meV/unit cell) [8], and lower than those of several prevalent sliding ferroelectrics, such as bilayer 3R-MoS_2 (∼15 meV/unit cell) [15], $MoTe_2$ (∼ 20 meV/unit cell) [52], and CrI_3 (26.8 meV/unit cell) [29]. In contrast, path2 exhibits an energy barrier that is an order of magnitude higher than path1, highlighting the selectivity of interlayer sliding. Unlike sliding ferroelectrics with OP, such as bilayer h-BN, whose threefold-degenerate switching paths cannot be deterministi-

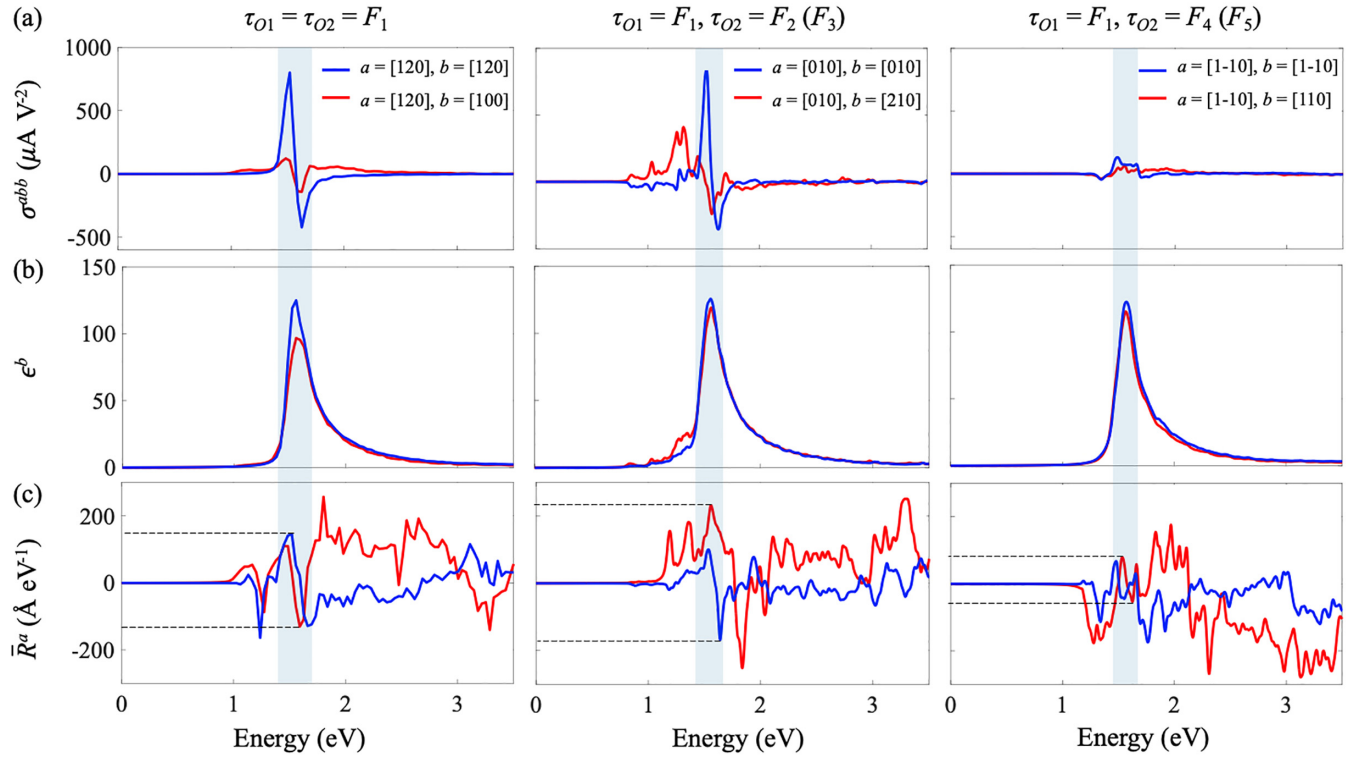

FIG. 3. (a) Shift current response σ^{abb}, (b) optical absorption ϵ^b, and (c) integrated shift vector $\bar{R}^a$ in the energy range of 0 to 3.5 eV for polar trilayer C_3N in different configurations. The blue regions highlight the energy range where the peaks of the optical absorption curves coincide with those of the shift current responses. The black dashed lines indicate the range of absolute values for the integrated shift vector within the blue regions.

cally controlled by an external electric field [53,54], a small in-plane electric field [29] is sufficient to achieve precise polarization switching in trilayer C_3N.

In addition to symmetry analysis, the origin of inversion-symmetry breaking and in-plane polarization can be further clarified through the charge density difference ($\Delta\rho$). Figure 2(d) shows the $\Delta\rho$ distributions on the slice corresponding to the middle layer S for different trilayer C_3N stacking configurations ($\tau_{O2} = F_1$, F_2, F_4, and F_6). Although the atomic structures of the middle layers are identical, different stacking orders induce distinct variations in $\Delta\rho$. As illustrated by the red lines in Fig. 2(d), the three polar structures ($\tau_{O2} = F_1$, F_2, and F_4) exhibit in-plane axial symmetry, consisting with the twofold rotation axes in their corresponding PGs. In contrast, the centrosymmetric configuration ($\tau_{O2} = F_6$) retains a well-defined inversion center, as indicated by the black pentagram in Fig. 2(d).

The IP usually plays a crucial role in enhancing BPVE for vdW layered materials [23,55–58]. For instance, stacking TMDs with BP can generate a spontaneous IP, thereby giving rise to an enhanced BPVE shift current [24,26]. Given this fact, the existence of IP in trilayer C_3N motivates us to further explore its BPVE properties. The shift current is the primary mechanism of BPVE, and its photoconductivity is described by a third-rank tensor [59]:

$$\sigma^{abb}(0;\omega,-\omega) = \frac{\pi e^3}{\hbar^2}\int \frac{d\mathbf{k}}{8\pi^3}\sum_{n,m} f_{nm}R^a_{nm}\left|r^b_{nm}\right|^2\delta(\omega_{mn}-\omega), \tag{3}$$

where a and b represent the directions of the photocurrent and linear polarized light polarization, respectively. f_{nm} and $\hbar\omega_{mn}$ are the Fermi-Dirac occupation numbers and energy difference between bands n and m, respectively. The terms r^b_{mn} and R^a_{nm} correspond to the dipole matrix element and the transition distance of an electron in real space after excitation, i.e., the shift vector. Figure 3(a) shows the shift current responses for trilayer C_3N in the energy range of 0 to 3.5 eV. Since the linearly polarized light is perpendicular to the 2D plane, b can either be parallel to a (blue lines) or perpendicular to a (red lines). The maximum shift current peaks are observed at 800 μA V^{-2} at 1.54 eV for $\tau_{O2} = F_1$, 838 μA V^{-2} at 1.53 eV for $\tau_{O2} = F_2$ (F_3), and 131 μA V^{-2} at 1.49 eV for $\tau_{O2} = F_4$ (F_5). These values are comparable to, or even larger than those observed in many emerging 2D polar materials that exhibit giant shift currents, such as ∼1000 μA V^{-2} in monolayer As [60], ∼ 800 μA V^{-2} in α-In_2Se_3 [61], ∼400 μA V^{-2} in $PtBi_2$ [62], and ∼300 μA V^{-2} in SnTe [63].

To understand the physical mechanism of the giant BPVE, we calculate the Brillouin zone-integrated $|r^b_{nm}|^2$ and R^a_{nm}, which correspond to the optical absorption $\epsilon^b = \frac{i\pi e^2}{\hbar}\int \frac{d\mathbf{k}}{8\pi^3}\sum_{n,m} f_{nm}|r^b_{nm}|^2\delta(\omega_{mn}-\omega)$ [Fig. 3(b)] and the integrated shift vector $\bar{R}^a = \frac{\Omega}{\hbar}\int \frac{d\mathbf{k}}{8\pi^3}\sum_{n,m} f_{nm}R^a_{nm}\delta(\omega_{mn}-\omega)$ [Fig. 3(c)], where Ω is the volume of the unit cell. As highlighted in the blue regions of Fig. 3, the peaks of the absorption curves coincide with those of the shift current responses, indicating that the dipole matrix term r^b_{mn} plays a decisive role in governing the BPVE. On the other hand, the

integrated shift vector $\bar{R}^a$ in the blue regions for the $\tau_{O2} = F_4$ (F_5) configurations is smaller compared to the other configurations, as indicated by the horizontal dashed lines in Fig. 3(c). This explains the relatively weaker shift current response for these two polar configurations. Such distinct shift current responses can thus serve as a fingerprint for identifying different polar configurations. The effects of stacking on the BPVE (see Fig. S14) are discussed in Sec. IV of Ref. [43].

IV. CONCLUSIONS

In summary, we have developed a general MSF theory for 2D materials with Bravais lattice symmetry. This theory generalizes the bilayer stacking ferroelectricity (BSF) framework to the full multilayer regime, providing systematic criteria for the emergence of polarization in multilayer stacking systems. Using the MSF theory, we have explained the onset of out-of-plane ferroelectricity in multilayer graphene and predicted that trilayer C_3N exhibits multidirectional in-plane ferroelectricity. Notably, the ferroelectric order in trilayer C_3N is coupled with the BPVE shift current, making this trilayer a promising platform for high-performance ferroelectric photovoltaic devices. Our work broadens the scope of sliding ferroelectricity, extending it to a wider class of systems, and underscores the critical role of layer number in tailoring the physical properties and functional potential of vdW stacking systems.

ACKNOWLEDGMENT

This work is supported by grants from the Fundamental Research Funds for the Central Universities (Grant No. 2024XKRC056) and the National Natural Science Foundation of China (Grant No. 12104037).

DATA AVAILABILITY

The data that support the findings of this article are not publicly available. The data are available from the authors upon reasonable request.

[1] A. Belianinov, Q. He, A. Dziaugys, P. Maksymovych, E. Eliseev, A. Borisevich, A. Morozovska, J. Banys, Y. Vysochanskii, and S. V. Kalinin, $CuInP_2S_6$ room temperature layered ferroelectric, Nano Lett. **15**, 3808 (2015).

[2] F. Liu, L. You, K. L. Seyler, X. Li, P. Yu, J. Lin, X. Wang, J. Zhou, H. Wang, H. He, *et al.*, Room-temperature ferroelectricity in $CuInP_2S_6$ ultrathin flakes, Nat. Commun. **7**, 12357 (2016).

[3] W. Ding, J. Zhu, Z. Wang, Y. Gao, D. Xiao, Y. Gu, Z. Zhang, and W. Zhu, Prediction of intrinsic two-dimensional ferroelectrics in In_2Se_3 and other III_2-VI_3 van der Waals materials, Nat. Commun. **8**, 14956 (2017).

[4] Y. Zhou, D. Wu, Y. Zhu, Y. Cho, Q. He, X. Yang, K. Herrera, Z. Chu, Y. Han, M. C. Downer, *et al.*, Out-of-plane piezoelectricity and ferroelectricity in layered α-In_2Se_3 nanoflakes, Nano Lett. **17**, 5508 (2017).

[5] C. Cui, W.-J. Hu, X. Yan, C. Addiego, W. Gao, Y. Wang, Z. Wang, L. Li, Y. Cheng, P. Li, *et al.*, Intercorrelated in-plane and out-of-plane ferroelectricity in ultrathin two-dimensional layered semiconductor In_2Se_3, Nano Lett. **18**, 1253 (2018).

[6] S. Yuan, X. Luo, H. L. Chan, C. Xiao, Y. Dai, M. Xie, and J. Hao, Room-temperature ferroelectricity in $MoTe_2$ down to the atomic monolayer limit, Nat. Commun. **10**, 1775 (2019).

[7] J. Gou, H. Bai, X. Zhang, Y. L. Huang, S. Duan, A. Ariando, S. A. Yang, L. Chen, Y. Lu, and A. T. S. Wee, Two-dimensional ferroelectricity in a single-element bismuth monolayer, Nature (London) **617**, 67 (2023).

[8] L. Li and M. Wu, Binary compound bilayer and multilayer with vertical polarizations: Two-dimensional ferroelectrics, multiferroics, and nanogenerators, ACS Nano **11**, 6382 (2017).

[9] M. Vizner Stern, Y. Waschitz, W. Cao, I. Nevo, K. Watanabe, T. Taniguchi, E. Sela, M. Urbakh, O. Hod, and M. Ben Shalom, Interfacial ferroelectricity by van der Waals sliding, Science **372**, 1462 (2021).

[10] K. Yasuda, X. Wang, K. Watanabe, T. Taniguchi, and P. Jarillo-Herrero, Stacking-engineered ferroelectricity in bilayer boron nitride, Science **372**, 1458 (2021).

[11] K. Yasuda, E. Zalys-Geller, X. Wang, D. Bennett, S. S. Cheema, K. Watanabe, T. Taniguchi, E. Kaxiras, P. Jarillo-Herrero, and R. Ashoori, Ultrafast high-endurance memory based on sliding ferroelectrics, Science **385**, 53 (2024).

[12] Z. Fei, W. Zhao, T. A. Palomaki, B. Sun, M. K. Miller, Z. Zhao, J. Yan, X. Xu, and D. H. Cobden, Ferroelectric switching of a two-dimensional metal, Nature (London) **560**, 336 (2018).

[13] Y. Wan, T. Hu, X. Mao, J. Fu, K. Yuan, Y. Song, X. Gan, X. Xu, M. Xue, X. Cheng, *et al.*, Room-temperature ferroelectricity in 1T'-ReS_2 multilayers, Phys. Rev. Lett. **128**, 067601 (2022).

[14] X. Wang, K. Yasuda, Y. Zhang, S. Liu, K. Watanabe, T. Taniguchi, J. Hone, L. Fu, and P. Jarillo-Herrero, Interfacial ferroelectricity in rhombohedral-stacked bilayer transition metal dichalcogenides, Nat. Nanotechnol. **17**, 367 (2022).

[15] P. Meng, Y. Wu, R. Bian, E. Pan, B. Dong, X. Zhao, J. Chen, L. Wu, Y. Sun, Q. Fu, *et al.*, Sliding induced multiple polarization states in two-dimensional ferroelectrics, Nat. Commun. **13**, 7696 (2022).

[16] S. Deb, W. Cao, N. Raab, K. Watanabe, T. Taniguchi, M. Goldstein, L. Kronik, M. Urbakh, O. Hod, and M. Ben Shalom, Cumulative polarization in conductive interfacial ferroelectrics, Nature (London) **612**, 465 (2022).

[17] Y. Liu, S. Liu, B. Li, W. J. Yoo, and J. Hone, Identifying the transition order in an artificial ferroelectric van der Waals heterostructure, Nano Lett. **22**, 1265 (2022).

[18] H. Jiang, L. Li, Y. Wu, R. Duan, K. Yi, L. Wu, C. Zhu, L. Luo, M. Xu, L. Zheng, *et al.*, Vapor deposition of bilayer 3R MoS_2 with room-temperature ferroelectricity, Adv. Mater. **36**, 2400670 (2024).

[19] X. Li, B. Qin, Y. Wang, Y. Xi, Z. Huang, M. Zhao, Y. Peng, Z. Chen, Z. Pan, J. Zhu, *et al.*, Sliding ferroelectric memories and synapses based on rhombohedral-stacked bilayer MoS_2, Nat. Commun. **15**, 10921 (2024).

[20] S. C. de la Barrera, Q. Cao, Y. Gao, Y. Gao, V. S. Bheemarasetty, J. Yan, D. G. Mandrus, W. Zhu, D. Xiao, and

B. M. Hunt, Direct measurement of ferroelectric polarization in a tunable semimetal, Nat. Commun. **12**, 5298 (2021).

[21] J. Liang, D. Yang, J. Wu, Y. Xiao, K. Watanabe, T. Taniguchi, J. I. Dadap, and Z. Ye, Resolving polarization switching pathways of sliding ferroelectricity in trilayer 3R-MoS_2, Nat. Nanotechnol. **20**, 500 (2025).

[22] R. Bian, R. He, E. Pan, Z. Li, G. Cao, P. Meng, J. Chen, Q. Liu, Z. Zhong, W. Li, *et al.*, Developing fatigue-resistant ferroelectrics using interlayer sliding switching, Science **385**, 57 (2024).

[23] J. Xin and Y. Guo, Bulk photovoltaic effect in the elemental blue phosphorus-based polar homojunction and heterojunction, J. Phys. Chem. C **128**, 9705 (2024).

[24] T. Akamatsu, T. Ideue, L. Zhou, Y. Dong, S. Kitamura, M. Yoshii, D. Yang, M. Onga, Y. Nakagawa, K. Watanabe, *et al.*, A van der Waals interface that creates in-plane polarization and a spontaneous photovoltaic effect, Science **372**, 68 (2021).

[25] R.-C. Xiao, Y. Gao, H. Jiang, W. Gan, C. Zhang, and H. Li, Non-synchronous bulk photovoltaic effect in two-dimensional interlayer-sliding ferroelectrics, npj Comput. Mater. **8**, 138 (2022).

[26] Z. Zeng, Z. Tian, Y. Wang, C. Ge, F. Strauß, K. Braun, P. Michel, L. Huang, G. Liu, D. Li, *et al.*, Dual polarization-enabled ultrafast bulk photovoltaic response in van der Waals heterostructures, Nat. Commun. **15**, 5355 (2024).

[27] L. Yang, S. Ding, J. Gao, and M. Wu, Atypical sliding and Moiré ferroelectricity in pure multilayer graphene, Phys. Rev. Lett. **131**, 096801 (2023).

[28] Y. Shan, Y. Li, D. Huang, Q. Tong, W. Yao, W.-T. Liu, and S. Wu, Stacking symmetry governed second harmonic generation in graphene trilayers, Sci. Adv. **4**, eaat0074 (2018).

[29] J. Ji, G. Yu, C. Xu, and H. J. Xiang, General theory for bilayer stacking ferroelectricity, Phys. Rev. Lett. **130**, 146801 (2023).

[30] J. Xin, Y. Guo, and Q. Wang, Enhanced theoretical framework for bilayer stacking ferroelectricity, Phys. Rev. B **111**, 224102 (2025).

[31] C. Kittel and P. McEuen, *Introduction to Solid State Physics* (John Wiley & Sons, New York, 2018).

[32] A. Singh, S. Xu, P. J. Sarsfield, P. D. Nunez, Z. Wang, S. Slizovskiy, N. Kay, J. Yin, Y. Mayamei, T. Taniguchi, *et al.*, Stacking-induced ferroelectricity in tetralayer graphene, arXiv:2504.07935.

[33] Z. Zhou, X. Peng, J. Bi, F. Xue, J. Jiang, H. Wu, Z. Shi, H. Qian, T. Kariyado, and S. Zhao, Optical imaging of spontaneous electric polarizations in tetralayer graphene, arXiv:2504.06874.

[34] S. S. Atri, W. Cao, B. Alon, N. Roy, M. V. Stern, V. Falko, M. Goldstein, L. Kronik, M. Urbakh, O. Hod, *et al.*, Spontaneous electric polarization in graphene polytypes, Adv. Phys. Res. **3**, 2300095 (2024).

[35] G. Kresse and J. Furthmüller, Efficient iterative schemes for *ab initio* total-energy calculations using a plane-wave basis set, Phys. Rev. B **54**, 11169 (1996).

[36] P. E. Blöchl, Projector augmented-wave method, Phys. Rev. B **50**, 17953 (1994).

[37] J. P. Perdew, K. Burke, and M. Ernzerhof, Generalized gradient approximation made simple, Phys. Rev. Lett. **77**, 3865 (1996).

[38] H. J. Monkhorst and J. D. Pack, Special points for Brillouin-zone integrations, Phys. Rev. B **13**, 5188 (1976).

[39] R. D. King-Smith and D. Vanderbilt, Theory of polarization of crystalline solids, Phys. Rev. B **47**, 1651 (1993).

[40] G. Henkelman, B. P. Uberuaga, and H. Jónsson, A climbing image nudged elastic band method for finding saddle points and minimum energy paths, J. Chem. Phys. **113**, 9901 (2000).

[41] J. Ibañez-Azpiroz, S. S. Tsirkin, and I. Souza, *Ab initio* calculation of the shift photocurrent by Wannier interpolation, Phys. Rev. B **97**, 245143 (2018).

[42] G. Pizzi, V. Vitale, R. Arita, S. Blügel, F. Freimuth, G. Géranton, M. Gibertini, D. Gresch, C. Johnson, T. Koretsune, *et al.*, Wannier90 as a community code: New features and applications, J. Phys.: Condens. Matter **32**, 165902 (2020).

[43] See Supplemental Material at http://link.aps.org/supplemental/10.1103/9tt5-qm26 for detailed group-theoretical analysis of MSF, including the constraint of τ_{O1} and τ_{O2} and the derivation of Eq. (1); MSF for all five categories of 2D materials with Bravais lattice symmetry; and electronic structures, stability, and BPVE of C_3N.

[44] F. Neumann, *Vorlesungen über die Theorie der Elasticität der festen Körper und des Lichtäthers* (B.G. Teubner, 1885).

[45] G. de la Flor, B. Souvignier, G. Madariaga, and M. I. Aroyo, Layer groups: Brillouin-zone and crystallographic databases on the bilbao crystallographic server, Acta Cryst. A **77**, 559 (2021).

[46] D. Çakır, C. Sevik, and F. M. Peeters, Significant effect of stacking on the electronic and optical properties of few-layer black phosphorus, Phys. Rev. B **92**, 165406 (2015).

[47] Z. Chen, H. Wang, and Z. Li, First-principles study of two dimensional C_3N and its derivatives, RSC Adv. **10**, 33469 (2020).

[48] J. Mahmood, E. K. Lee, M. Jung, D. Shin, H.-J. Choi, J.-M. Seo, S.-M. Jung, D. Kim, F. Li, M. S. Lah, *et al.*, Two-dimensional polyaniline (C_3N) from carbonized organic single crystals in solid state, Proc. Natl. Acad. Sci. USA **113**, 7414 (2016).

[49] B. Mortazavi, Ultra high stiffness and thermal conductivity of graphene like C_3N, Carbon **118**, 25 (2017).

[50] J. Xu, J. Mahmood, Y. Dou, S. Dou, F. Li, L. Dai, and J.-B. Baek, 2D frameworks of C_2N and C_3N as new anode materials for lithium-ion batteries, Adv. Mater. **29**, 1702007 (2017).

[51] W. Wei, S. Yang, G. Wang, T. Zhang, W. Pan, Z. Cai, Y. Yang, L. Zheng, P. He, L. Wang, *et al.*, Bandgap engineering of two-dimensional C_3N bilayers, Nat. Electron. **4**, 486 (2021).

[52] Z. Lin, C. Si, S. Duan, C. Wang, and W. Duan, Rashba splitting in bilayer transition metal dichalcogenides controlled by electronic ferroelectricity, Phys. Rev. B **100**, 155408 (2019).

[53] Q. Yang and S. Meng, Light-induced complete reversal of ferroelectric polarization in sliding ferroelectrics, Phys. Rev. Lett. **133**, 136902 (2024).

[54] J. Wang, X. Li, X. Ma, L. Chen, J.-M. Liu, C.-G. Duan, J. Íñiguez-González, D. Wu, and Y. Yang, Ultrafast switching of sliding polarization and dynamical magnetic field in van der Waals bilayers induced by light, Phys. Rev. Lett. **133**, 126801 (2024).

[55] Y. Dong, M.-M. Yang, M. Yoshii, S. Matsuoka, S. Kitamura, T. Hasegawa, N. Ogawa, T. Morimoto, T. Ideue, and Y. Iwasa, Giant bulk piezophotovoltaic effect in 3R-MoS_2, Nat. Nanotechnol. **18**, 36 (2023).

[56] Y. Gao, M. Yang, W. Zou, J. Zhou, and C. Zhang, Band-edge mixture engineered giant and switchable shift current generation, Nano Lett. **24**, 12560 (2024).

[57] H. Zhou, Y. Wei, W. Luo, C. Tan, Z. Dou, Z. Hu, Q. Li, and X. Zheng, Symmetry-breaking-engineered in-plane bulk photovoltaic effect in van der Waals WS_2/CrOCl heterostructure, RSC Adv. **15**, 25625 (2025).

[58] C. Hou, J. Xin, Y. Shen, Y. Guo, and Q. Wang, Giant bulk photovoltaic effect in penta-$PdTe_2$ induced by layer stacking, J. Phys. Chem. Lett. **16**, 7177 (2025).

[59] J. E. Sipe and A. I. Shkrebtii, Second-order optical response in semiconductors, Phys. Rev. B **61**, 5337 (2000).

[60] Z. Qian, J. Zhou, H. Wang, and S. Liu, Shift current response in elemental two-dimensional ferroelectrics, npj Comput. Mater. **9**, 67 (2023).

[61] R. P. Tiwari, B. Birajdar, and R. K. Ghosh, First-principles calculation of shift current bulk photovoltaic effect in two-dimensional α-In_2Se_3, Phys. Rev. B **101**, 235448 (2020).

[62] L. Yang, L. Li, Z.-M. Yu, M. Wu, and Y. Yao, Two-dimensional topological ferroelectric metal with giant shift current, Phys. Rev. Lett. **133**, 186801 (2024).

[63] G. Jin and L. He, Peculiar band geometry induced giant shift current in ferroelectric SnTe monolayer, npj Comput. Mater. **10**, 23 (2024).